

Non-spherical bubble collapse near rigid and compliant surfaces

S. Alahyari Beig, M. Rodriguez and E. Johnsen
 (University of Michigan, Ann Arbor, MI, USA)

ABSTRACT

The inertial collapse of cavitation bubbles is known to be capable of damaging its surroundings whether rigid or compliant. In order to explore this phenomenon, we leverage a novel numerical approach to investigate the dynamics of shock-induced collapse of (i) a single bubble, and (ii) multiple bubbles near rigid and compliant objects. Our Eulerian method is high-order accurate and captures discontinuities (shock waves and interfaces) in a stable fashion. We characterize the pressure and temperature fields based on the relevant non-dimensional parameters entering the problem. In particular, we show that bubble collapse causes temperature rises in neighboring solid objects via two mechanisms: the shock produced at collapse and heat diffusion from the hot bubble close to the solid surface. We use a newly developed analytical thermal model to predict the temperature distribution within the neighboring surface. A numerical model that accounts for the viscoelasticity of a compliant object is also used to study its interactions with the fluid flow. Finally, we quantify the effects of bubble-bubble interactions on collapse dynamics for multiple bubbles and cavitation-induced damage.

1 INTRODUCTION

Cavitation bubble dynamics appear in a wide range of hydraulic applications, such as turbomachinery, naval structures, biomedical ultrasound, combustion, and neutron scattering. By contrast to boiling in which liquid vaporizes as the temperature is increased, cavitation happens due to local pressure changes in a liquid, leading to the formation of vapor bubbles. When subjected to higher pressure regions, these bubbles implode, thus generating shock waves, and transient regions of high pressure and temperature. One of the important consequences of cavitation is the structural damage to neighboring surfaces due to bubble collapse (Kornfeld & Suvorov, 1944; Knapp, 1955; Benjamin & Ellis, 1966; Tomita *et al.*, 1986; Philip &

Lauterborn, 1998; Lindau & Lauterborn, 2003; Franc *et al.*, 2012).

The propagation of shock and rarefaction waves in a multiphase medium interacting with solid boundaries results in a particularly complicated multiscale and multiphysics problem. Although this problem has been investigated over the past years, it is still an obscure phenomenon and many fundamental questions regarding the complex dynamics of this flow, its detailed damage mechanisms, and mitigation strategies have yet to be answered. The modern description of cavitation erosion to metallic surfaces is based on a sequence of four steps (Kim *et al.*, 2014): production of small-scale vapor structures, impact loads due to bubble collapse, pitting, and failure. According to this model, cavitation erosion originates from the mechanical loading produced on the material which is dependent on the local bubble dynamics. It is unclear whether such a model holds for cavitation damage to soft material, such as Polyurea, proposed for blast mitigation (Samiee *et al.*, 2013), and other polymer based materials. In this work, we will study the thermal and mechanical loading effects of bubbles collapsing near rigid and viscoelastic materials.

Although the pressures and stresses produced by this process have been investigated particularly, less is known about heating of the surrounding medium, which may be important when collapse occurs near objects whose mechanical properties strongly depend on temperature (e.g., soft materials). Recent experiments suggest that high temperatures produced by bubble collapse near compliant surfaces influence the damage mechanism(s) (Hattori *et al.*, 2015).

Moreover, the influence of the shock wave on soft materials and the response of the material on the shock wave and bubble dynamics are poorly understood in these experiments. One challenge lies in the non-trivial implementation of constitutive models describing the material that include effects such as (non-linear) elasticity, history and viscosity. Studies have shown that these soft materials can have a viscoelastic response (Qiao *et al.*, 2011).

Due to the complexity of the physics and the wide

range of spatial and temporal scales in cavitation, numerical simulations have emerged as a reliable tool to complement analytical and experimental studies. Early simulations of such flows implemented incompressible approaches to predict the initial behavior of the bubble (Blake & Gibson, 1987). However, such methods break down in the stages of the collapse when compressibility effects become important. In the past few years, researchers have been focusing on developing algorithms capable of simulating these flows by solving the Euler equations in a compressible framework in order to handle shock waves, contacts and material interfaces (Ball *et al.*, 2000; Nourgaliev *et al.*, 2006; Johnsen & Colonius, 2006; Hawker & Ventikos, 2012; Coralic & Colonius, 2014). These algorithms tend to be computationally expensive and complicated to code. They also bring about other numerical difficulties, such as the generation of pressure and temperature oscillations across the material discontinuities for interfacial flows, which limit the usability of these methods (Abgrall, 1996; Shyue, 1998; Johnsen & Ham, 2012; Beig & Johnsen, 2015). To overcome these issues, we have developed a novel numerical multiphase model to conduct efficient and accurate simulations by solving the three-dimensional compressible Navier-Stokes equations for a binary gas-liquid system (Beig & Johnsen, 2015; Beig *et al.*, 2015).

Viscoelasticity introduces further complications. To study the bubble dynamics near or in viscoelastic materials, models, based on the Rayleigh-Plesset equation (Fogler & Goddard, 1970; Tanasawa & Yang, 1970), have been recently developed and were extended to include elasticity (Yang & Church, 2005; Hua & Johnsen, 2013; Gaudron *et al.*, 2015). However, these approaches are limited by the assumptions that the bubble dynamics are spherically symmetric and that the near-field flow is incompressible.

These assumptions break down in the last stages of the violent and non-spherical collapse of a gas bubble near a rigid or compliant object. Thus, the compliant solid's viscoelastic constitutive relation must account for the strains (or deformations), typically described in a Lagrangian specification, in a feasible Eulerian formulation for capturing discontinuities. In the present effort, the Jaumann derivative of the elastic terms in the Kelvin-Voigt viscoelastic constitutive relation is performed, which effectively transforms strains into strain rates (Rodriguez & Johnsen, 2016). These strain rates can then be computed in an Eulerian formulation since they are proportional to velocity gradients (Kulikovskii *et al.*, 2002). As a result, a set of evolution equations for the elastic components of the stress tensor are introduced alongside the mul-

tiphase model equations.

The objective of the present work is to better understand the potential damage caused by the shock-induced collapse of individual bubbles near rigid and compliant objects. We provide three- and two-dimensional numerical simulations of this problem for different geometrical configurations to investigate the basic flow physics. Three-dimensional numerical simulations are used to specifically study the temperature effects near a solid surface. We demonstrate that significant maximum wall temperatures can be achieved, depending on the heat diffusivity of the material. We further study the viscoelastic effects of the compliant object through two-dimensional simulations. We show that the mismatch between the acoustic impedance of the compliant object and surrounding fluid can affect collapse dynamics and result in non-negligible deformations of the neighboring object. In addition, we investigate the effects of bubble-bubble interactions on dynamics of collapsing bubbles and demonstrate that these interactions might significantly affect the pressures and temperatures produced by the collapse. This study will deepen our knowledge of the detailed physics of collapse of bubble clouds, and eventually help us formulate a more accurate mixture model, while current models do not consider the effects of bubble-bubble interactions.

2 PHYSICAL AND NUMERICAL MODELS

The numerical methods presented in this article are based on the work of Beig & Johnsen (2015) and Rodriguez & Johnsen (2016).

2.1 GOVERNING EQUATIONS

The equations governing the multiphase flows of interest, are:

$$\frac{\partial \rho}{\partial t} + \frac{\partial}{\partial x_j}(\rho u_j) = 0, \quad (1a)$$

$$\frac{\partial}{\partial t}(\rho u_i) + \frac{\partial}{\partial x_j}(\rho u_i u_j - \sigma_{ij}) = 0, \quad (1b)$$

$$\frac{\partial E}{\partial t} + \frac{\partial}{\partial x_j}(E u_j - \sigma_{ij} u_i) = -\frac{\partial Q_k}{\partial x_k}, \quad (1c)$$

where ρ is the mixture density, u_i the velocity vector, σ_{ij} the Cauchy stress tensor, $E = \rho e + \frac{1}{2} \rho u_k^2 + \rho e^{(e)}$ the total energy, ρe the internal energy (per unit volume), δ_{ij} the identity tensor, and, if present, the elastic energy $\rho e^{(e)}$ is expressed in terms of the deviatoric elastic stresses. Surface tension and mass transfer are

not expected to change the collapse dynamics, since the time scale of the flow is relatively short and the fluids are assumed to be immiscible; therefore, these effects are neglected. The heat flux Q_j is given by Fourier's law:

$$Q_j = -\kappa \frac{\partial T}{\partial x_j}, \quad (2)$$

where κ is the heat conductivity and T the temperature. To define the Cauchy stress tensor, the strain-rate and deviatoric strain-rate tensors (applicable for infinitesimal deformations) are defined,

$$\dot{\epsilon}_{ij} = \frac{1}{2} \left(\frac{\partial u_i}{\partial x_j} + \frac{\partial u_j}{\partial x_i} \right), \quad \dot{\epsilon}_{ij}^{(d)} = \dot{\epsilon}_{ij} - \frac{1}{3} \dot{\epsilon}_{kk} \delta_{ij}.$$

Additionally, the Cauchy stress tensor can be written in terms of isotropic and deviatoric contributions, $\sigma_{ij} = \sigma_{ij}^{(i)} + \tau_{ij}^{(d)}$. The isotropic term consists of mechanical pressure and bulk viscous contributions:

$$\sigma_{ij}^{(i)} = -p \delta_{ij} + \mu_B \dot{\epsilon}_{kk} \delta_{ij}, \quad (3)$$

where μ_B is the bulk viscosity and p the pressure. Now the Cauchy stress tensor is fully defined using Kelvin-Voigt model, the simplest linear constitutive relation that accounts for the relaxation, elastic and viscous effects, for the deviatoric contribution:

$$\tau_{ij} = \mu_B \dot{\epsilon}_{kk} + 2\mu_s \dot{\epsilon}_{ij}^{(d)} + 2G \epsilon_{ij}^{(d)}, \quad (4)$$

where μ_s is the shear viscosity and G is the shear modulus. The deviatoric elastic contribution in the Kelvin-Voigt model, $\tau_{ij}^{(e)} = 2G \epsilon_{ij}^{(d)}$, is then used to calculate the elastic energy: $\rho e^{(e)} = \tau_{ij}^{(e)} \tau_{ij}^{(e)} / 4G$. This model has the advantage of reducing to the Newtonian fluid for $G = 0$. The Newtonian fluid and Kelvin-Voigt viscoelastic solid will be used in this work for the solid and compliant object simulations, respectively.

To close the system, a relation between pressure, temperature and internal energy valid for gases and liquids is required. For this purpose, the stiffened equation of state described in detail by Le Metayer *et al.* (2005) is a simple and sufficiently accurate model, which has been validated against experiments for shock propagation in water and certain solids, and has been used to simulate cavitating flows. The relationships between pressure, temperature and internal energy are given by:

$$\rho(e - q) = \frac{p}{n-1} + \frac{nB}{n-1} = \rho c T + B, \quad (5)$$

where n , B , q , and c are material properties fit to experimental data. For air and water, the relevant

constants take the values shown in Table 1. The coefficients corresponding to polyurea are chosen such that the appropriate sound speed (2039 m/s) and shear modulus (20 GPa) reported in literature are obtained (Amini *et al.*, 2010).

2.2 STRESS-EVOLUTION MODEL

We consider the Kelvin-Voigt model, in which the viscous and elastic contributions are simply added to form the total deviatoric stress. Inspired by Kulikovskii *et al.* (2002); Gavrilyuk *et al.* (2008), a temporal derivative (Jaumann in our work) of the elastic stress tensor is taken to eliminate strains, whose advective fluxes can be re-arranged into divergence form using mass conservation Rodriguez & Johnsen (2016):

$$\begin{aligned} \frac{\partial}{\partial t} (\rho \tau_{ij}^{(e)}) + \frac{\partial}{\partial x_j} (\rho \tau_{ij}^{(e)} u_j) = \rho \left[\omega_{ik} \tau_{kj}^{(e)} \right. \\ \left. - \tau_{ik}^{(e)} \omega_{kj} + 2G \left(\dot{\epsilon}_{ij} - \frac{1}{3} \dot{\epsilon}_{kk} \delta_{ij} \right) \right], \end{aligned} \quad (6)$$

where $\omega_{ik} = \frac{1}{2} \left(\frac{\partial u_i}{\partial x_k} - \frac{\partial u_k}{\partial x_i} \right)$. The rotational terms are necessary to preserve objectivity. Thus, in two dimensions, three additional equations must be solved for the elastic contributions of stress ($\tau_{11}^{(e)}$, $\tau_{22}^{(e)}$ and $\tau_{12}^{(e)}$). In the absence of elastic effects (i.e., $G = 0$), the compressible Navier-Stokes equations are recovered, in which case the viscous stresses are computed explicitly.

2.3 MULTIPHASE MODEL

In order to introduce multiple phases, we need to solve additional mass conservation equations. For instance, the following equation describes this physical principle in a two-phase system:

$$\frac{\partial(\rho z)}{\partial t} + \frac{\partial}{\partial x_j} (\rho z u_j) = 0, \quad (7)$$

where z is the mass fraction of one of the phases. Using shock-capturing schemes leads to spurious pressure oscillations and temperature errors at interfaces.

Table 1: Relevant constants for the stiffened equation of state.

Parameter	Air	Water	Polyurea
n	1.4	2.35	2.35
B [GPa]	0	1	2.1
c [kJ/kg K]	0.718	1.816	4.34
q [kJ/kg]	0	-1.167	-1.167

To address these problems, we simultaneously solve equations for the volume fraction α of the corresponding phase in conservative,

$$\frac{\partial(\rho^{(k)}\alpha^{(k)})}{\partial t} + \frac{\partial}{\partial x_j} \left(\rho^{(k)}\alpha^{(k)}u_j \right) = 0, \quad (8)$$

and non-conservative,

$$\frac{\partial\alpha^{(k)}}{\partial t} + u_j \frac{\partial\alpha^{(k)}}{\partial x_j} = \Gamma \frac{\partial u_j}{\partial x_j}, \quad (9)$$

forms, where

$$\Gamma = \alpha^{(1)}\alpha^{(2)} \frac{\rho^{(2)}(a^{(2)})^2 - \rho^{(1)}(a^{(1)})^2}{\alpha^{(1)}\rho^{(2)}(a^{(2)})^2 + \alpha^{(2)}\rho^{(1)}(a^{(1)})^2}. \quad (10)$$

To prevent pressure oscillations, the pressure must be computed as follows:

$$p = \left[\rho e - \sum_k \alpha^{(k)} \left(\frac{nB}{n-1} \right)^{(k)} - \sum_k \rho^{(k)}\alpha^{(k)}q^{(k)} \right] / \sum_k \alpha^{(k)} \left(\frac{1}{n-1} \right)^{(k)}. \quad (11)$$

To prevent temperature errors, the temperature must be computed as follows:

$$T = \left[\rho e - \sum_k \alpha^{(k)} B^{(k)} - \sum_k \rho^{(k)}\alpha^{(k)}q^{(k)} \right] / \sum_k \rho^{(k)}\alpha^{(k)}c^{(k)}. \quad (12)$$

In Eqs. (11) and (12), $\rho^{(k)}\alpha^{(k)}$ is computed from the conservative form and $\alpha^{(k)}$ is computed from the non-conservative form of the transport equation.

2.4 NUMERICAL METHOD

For the simulations presented in this work, time marching is handled with a third-order accurate explicit strong stability preserving Runge-Kutta scheme (Gottlieb & Shu, 1996). The time step is adaptively set to satisfy the advection and diffusion constraints, with CFL=0.8 and VNN=0.4. For the spatial discretization, a solution-adaptive high-order accurate central difference/discontinuity-capturing method is proposed (Movahed & Johnsen, 2013; Henry de Frahan *et al.*, 2015). This method can represent both broadband flow motions and discontinuities accurately and efficiently. The basic idea is that non-dissipative methods are used where the solution is smooth, while the more dissipative and computationally expensive capturing schemes are applied near discontinuous regions. For this purpose, a discontinuity

sensor discriminates between smooth and discontinuous (shocks, contacts and interfaces) regions; smooth regions are computed using central differences, and the approach of Johnsen & Colonius (2006) is used to handle the discontinuities.

2.5 COMPARISON TO KNOWN SOLUTIONS

We compare our numerical results with theoretical results. Fig. 1 shows the radius of the bubble, and temperature of the bubble center as a function of time with a Keller-Miksis (KM) solution of the Rayleigh collapse of an isolated gas bubble in water subjected to a pressure ratio of 43.

KM is an established model and has been validated against experiments in the literature (Keller & Miksis, 1980; Lauterborn & Kurz, 2010; Brenner *et al.*, 2002), and this comparison verifies that our simulation is capturing the right physics of spherical bubble dynamics problems, including the calculation of the temperature. Fig. 1 shows a good agreement with the KM model which assures the consistency of our simulations. In particular, we note that neglecting the source term in Eq. (9), which is routinely done in the literature (Coralic & Colonius, 2014), does not represent the compressible multiphase flow accurately and would require significantly higher resolutions. The spikes in the temperature plot are caused by the shock released from the discontinuous initial conditions bouncing back and forth within the collapsing bubble that cannot be captured with a homobaric model such as KM.

We also compare our simulations of the shock-induced collapse of a two-dimensional cavity with the analogous experiments by Bourne & Field (1992). A viscoelastic, gel-like medium is the surrounding fluid instead of a Newtonian fluid, typically water. The Kelvin-Voigt model is used to represent the viscoelastic medium. The material properties of the

Table 2: Comparisons between the Bourne & Field (1992) experiments (Exp.) and present numerical (Num.) results.

Shock pressure (GPa)	Jet velocity (m/s)		Collapse time (μs)	
	Exp.	Num.	Exp.	Num.
0.5	1500 \pm 400	1530	5 \pm 1	5.8
1.9	3300 \pm 300	2861	1.8 \pm 0.2	2.7
3.5	8000 \pm 4000	3817	1 \pm 0.5	2

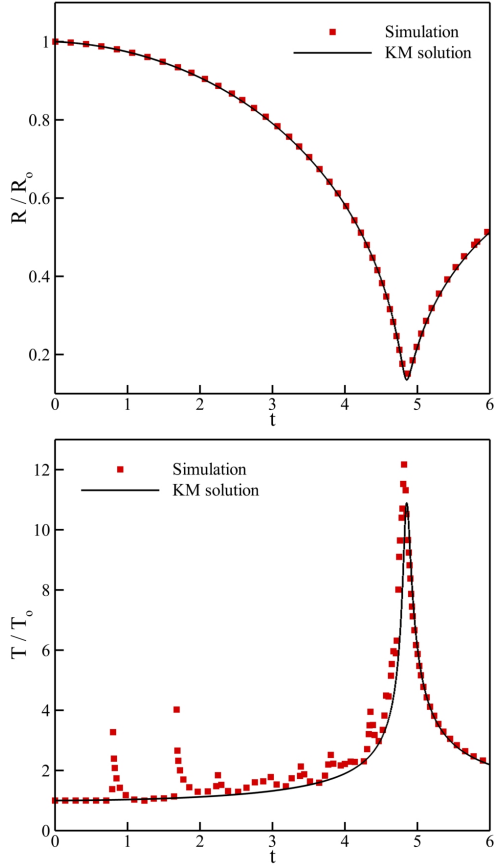


Figure 1: The evolution of radius (top) and temperature (bottom) in time for Rayleigh collapse of an isolated bubble with 128 points per initial bubble radius.

gel are comparable with the experiments. To match the experimental initial conditions, a shock wave is implemented into the simulation, which matches the Rankine-Hugoniot conditions. The resolution for all the cases was such that there were 256 points per initial bubble radius. The gel properties were approximated: $\rho = 970 \text{ kg/m}^3$, $n = 2.35$, $B = 1 \text{ GPa}$, $\mu_B = \mu_s = 50 \text{ mPa s}$, and $G = 8.35 \text{ kPa}$. In Table 2, we compare the re-entrant jet velocity and bubble diameter collapse time with the experimental results. We note that the 6 mm cavity diameter cases show agreement with experiments. For these parameters, we note that viscoelasticity does not play a significant role on the dynamics.

3 RESULTS AND DISCUSSION

We carry out three- and two-dimensional simulations of shock-induced collapse of (i) a single bubble, and (ii) multiple bubbles near a rigid surface and com-

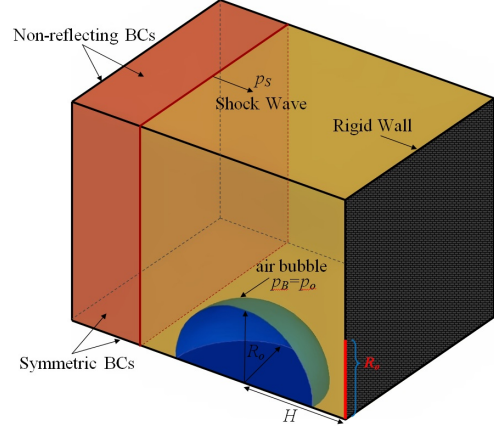


Figure 2: Problem set-up for the shock-induced collapse of an initially spherical gas bubble near a rigid surface.

pliant object. The compressible Navier-Stokes equations are solved for the simulations using the multi-phase model in section 2. For the compliant object, the additional equations for the Kelvin-Voigt model, Eq. (6), are solved. Unless otherwise mentioned, we use the ambient temperature 300 K, the initial bubble radius $200 \mu\text{m}$, and the density and sound speed of air at that temperature to non-dimensionalize all quantities. Additionally, unless otherwise mentioned, the shock wave is initialized using the Rankine-Hugoniot conditions in the appropriate medium for a pressure ratio of 300 and a stand-off distance from the bubble center to the neighboring surface of $H/R_o = 1.125$. For the problems with the compliant object, the compliant object thickness is $T/R_o = 2$.

3.1 SINGLE-BUBBLE COLLAPSE

In this section, we perform three-dimensional simulations of a single-bubble collapsing near a rigid surface, and implement a novel analytical thermal model to assess the temperature effects on the surface damage. We also carry out two-dimensional simulations of single-bubble collapse near a compliant object in order to study the effects of collapse dynamics on the deformation of the neighboring object.

3.1.1 3D SIMULATIONS OF SINGLE-BUBBLE COLLAPSE NEAR A RIGID WALL

We consider the collapse of an initially spherical bubble in equilibrium with its surroundings, located at a distance H away from a rigid wall. The schematic of the problem setup is shown in Fig. 2. A shock wave propagating toward the wall impinges upon the bubble and causes its collapse.

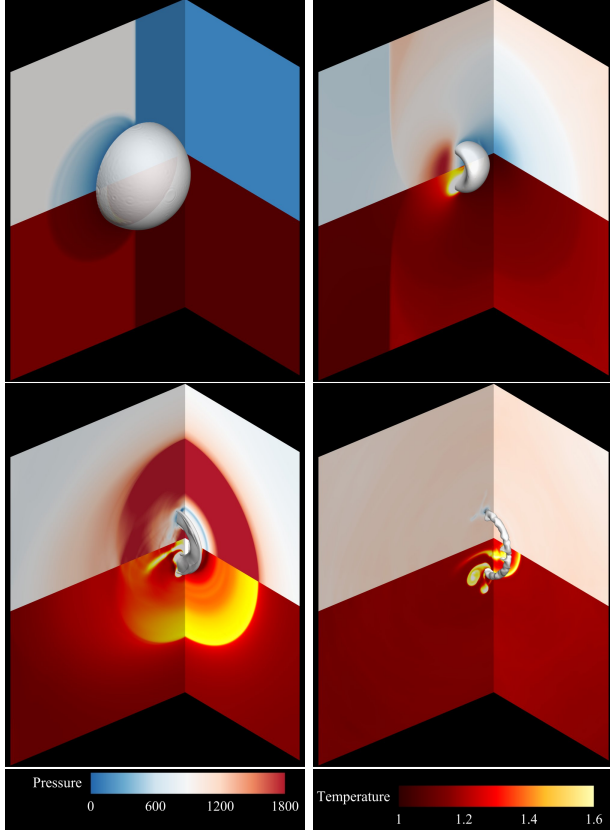


Figure 3: Pressure (top) and temperature (bottom) contours for the 3D shock-induced bubble collapse base problem.

In this case, we only simulate one quarter of the bubble due to the axisymmetry. We use a uniform Cartesian grid with the resolution of $1024 \times 768 \times 768$ (256 cells per bubble radius at $t = 0$).

Fig. 3 shows four different frames of the collapse process. It can be seen that the right-moving shock interacts with the bubble, thus producing a reflected rarefaction wave (frame 1). As the bubble starts its collapse, the incoming shock hits the rigid wall and reflects back onto the bubble. This doubles the surrounding pressure and enhances the collapse (frame 2). During the collapse, a re-entrant jet directed toward the wall is produced, which, upon impact with the distal side, generates an outward propagating shock (frame 3). Thereafter, the bubble takes the form of a vortex ring, which is hot due to the rapid compression and is convected toward the wall (frame 4). This process produces regions of high pressure and temperature along the wall, and deliver a significant amount of energy into the neighboring surface, which may enhance the structural damage.

Although the pressures produced during this pro-

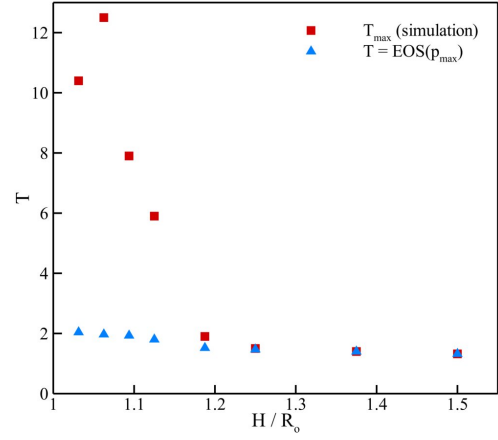


Figure 4: Wall temperature; red square: maximum flow temperature measured on the wall; blue delta: temperature corresponding to the shock wave from the collapse.

cess have been studied well in the literature (Ball *et al.*, 2000; Nourgaliev *et al.*, 2006; Johnsen & Colonius, 2009), temperature changes have remained unpredicted in simulations due to numerical challenges (Beig & Johnsen, 2015). Our simulations indicate that two mechanisms raise the temperature of the neighboring wall: the strong radial shock wave produced at the collapse, and the heat diffusion from the hot vortex ring convecting toward the wall. To illustrate these competing mechanisms, we plot the maximum flow temperature measured on the wall and the maximum temperature corresponding to the shock wave from the collapse (computed using the pressure of the shock wave and the stiffened EOS for water) for different values of H/R_o in Fig. 4. This figure shows that for the cases where the bubble is initially close to the wall ($H/R_o < 1.25$), the maximum measured temperature is higher than the shock temperature. This indicates that the source for the high temperatures on the surface of the wall is not the shock wave, but the hot vortex ring contacting the wall surface; only the air bubble can get that hot. On the other hand, in the cases where the bubble is initially located far from the wall, the maximum temperature is caused by the shock wave from the collapse.

This behavior can be examined by plotting pressure and temperature along the wall (the red line in Fig. 2) for two different configurations (close and far initial location of the bubble from the wall). Johnsen & Colonius (2009) showed that the closer bubble to the wall leads to a faster and stronger collapse. We know that the maximum temperature in the whole domain appears inside the air bubble at the collapse time where the minimum bubble volume and

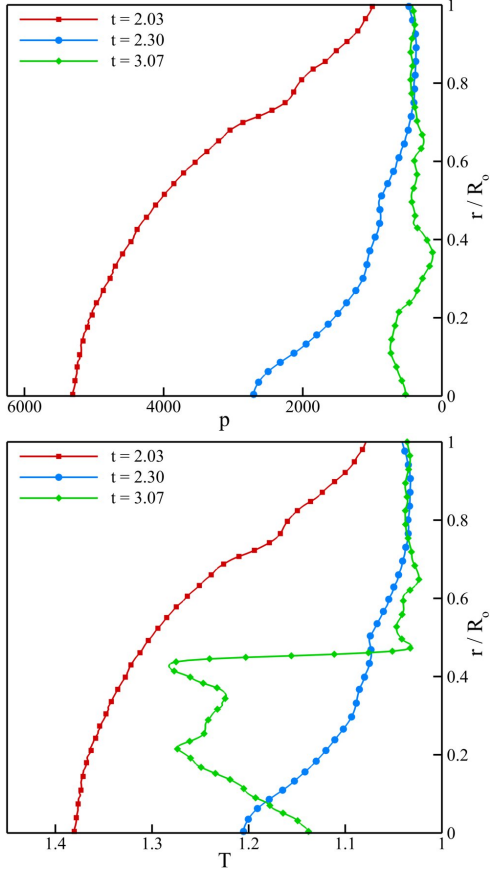


Figure 5: Pressure (top) and temperature (bottom) plots along the wall after the collapse for $H/R_o = 1.37$.

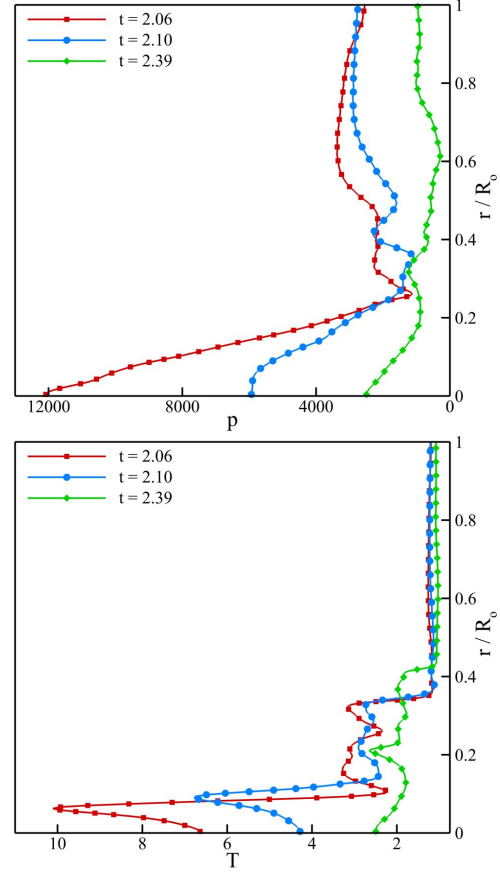


Figure 6: Pressure (top) and temperature (bottom) plots along the wall after the collapse for $H/R_o = 1.03$.

the maximum pressure are experienced. After the collapse, the pressure decreases rapidly and bubble starts to grow. This results in an immediate reduction in bubble temperature, implying that as the initial proximity of the bubble with respect to wall gets smaller, its maximum temperature becomes higher, and subsequently the hot vortex ring reaches the wall closer to the time that collapse happens. This process leads to higher temperatures on the surface of the solid boundary.

Fig. 5 shows pressure and temperature along the wall at three different times after the collapse for the case where the initial location of the bubble is relatively far from the wall ($H/R_o = 1.37$). It can be seen that at early times after the collapse, the pressure and temperature plots follow the same pattern meaning that they have the same source. Therefore the mechanism creating high pressures (the shock wave from the collapse) is the source for the temperature profile as well. Discrepancies between the two plots emerge over time: the temperature is higher than what was

expected for $r/R_o < 0.45$. The temperature of the affected region is increased due to the hot vortex ring reaching the wall surface. Since the initial bubble stand-off distance is relatively large, it takes a longer time for the vortex ring to reach the wall surface. Because of the short time scale of the flow, it is sufficient for the bubble to cool down from thousands of degrees at the collapse time to less than 400 K when it contacts the wall surface.

Fig. 6 plots pressure and temperature along the same line on the wall for the case where the bubble is initially located close to the wall ($H/R_o = 1.03$). In contrast with Fig. 5, the discrepancies between pressure and temperature plots can be seen even at early times after collapse. This indicates that the source of high pressure is different from the source of high temperature. The high pressures are caused by the shock wave and/or water hammer effect from the collapse. Assuming that there is no contact between the hot air and the solid surface, those pressures cannot lead to the high temperatures in the liquid, which means

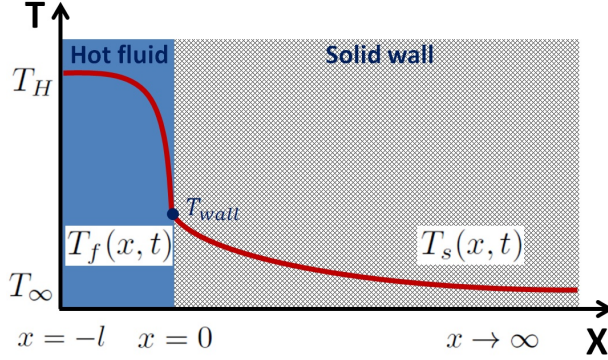


Figure 7: Schematic of the thermal boundary layer between the hot flow and the solid wall.

that the vortex ring is definitely contacting the wall surface. Figs. 5 and 6 explain the importance of the initial proximity of the bubble with respect to the wall on the temperature of the wall surface.

3.1.2 ANALYTICAL THERMAL MODEL

The simulations presented in section 3.1.1 show that when a bubble collapses close to a neighboring solid, significant rise in the flow temperature touching the solid surface is achieved. However, these temperatures are not the actual temperature of the surface: there exists a thin thermal boundary layer between the solid surface and the hot fluid covering it that can never be captured in finite-resolution simulations (shown in Fig. 7). To estimate the actual temperature of the wall surface, we analytically solve a simplified model problem based on the data from our high-fidelity simulations.

We start with the one-dimensional heat diffusion equation for each medium:

$$\frac{\partial T_k}{\partial t} = \alpha_k \frac{\partial^2 T_k}{\partial x^2}, \quad (13)$$

where α is the thermal diffusivity and $k \equiv \{f, s\}$ defines fluid and solid, respectively. We need to solve this equation for both the fluid and solid, coupled through the boundary conditions at the interface between the two media. These conditions imply that at $x = 0$ the temperature profile must be continuous, meaning that $T_f(0, t) = T_s(0, t)$, and the heat transfer occurs only between the solid and the fluid, which further implies that that

$$k_f \frac{\partial T_f}{\partial x} = k_s \frac{\partial T_s}{\partial x}. \quad (14)$$

In addition, the temperature of the solid at infinity is fixed to a constant temperature, $T_s(\infty, t) = T_\infty$, and

for the fluid we have $T_f(-l, t) = T_H(t_i)$. It should be pointed out that T_H comes from our numerical simulations, and therefore, is a discrete function of time and space. This means that Eq. (13) must be solved for every grid cell that shares an interface with the solid boundary during the simulation time, and l is the width of the corresponding cell. This problem is temporal, so solving the equations requires appropriate initial conditions (at the beginning of each time step) as well. For the fluid part, since T_H is the cell-averaged temperature of the cell neighboring the wall, it is reasonable to assume that $T_f(x, 0) = T_H(t_i)$ at the beginning of each time-step. While for the solid part, this assumption is not valid except for the very first time-step where the temperature inside the solid boundary is uniform $T_s(x, 0) = T_\infty$. Accordingly, the following temperature profiles can be achieved analytically for the first time-step:

$$T_f(x, t) = T_H + \frac{T_H - T_\infty}{1 + \sigma} \left\{ \sum_{n=0}^{\infty} \beta^n \left[\operatorname{erfc} \left(\frac{2(n+1)l + x}{2\sqrt{\alpha_f t}} \right) - \operatorname{erfc} \left(\frac{2nl - x}{2\sqrt{\alpha_f t}} \right) \right] \right\}, \quad (15)$$

$$T_s(x, t) = T_\infty + \frac{(T_H - T_\infty)\sigma}{1 + \sigma} \left[\operatorname{erfc} \left(\frac{\gamma x}{2\sqrt{\alpha_f t}} \right) + (\beta + 1) \sum_{n=1}^{\infty} \beta^{n-1} \operatorname{erfc} \left(\frac{2nl + \gamma x}{2\sqrt{\alpha_f t}} \right) \right], \quad (16)$$

where $\gamma = \sqrt{\alpha_f/\alpha_s}$, $\sigma = k_f/k_s \sqrt{\alpha_f/\alpha_s}$, and $\beta = (1 - \sigma)/(1 + \sigma)$.

Despite the initial condition at $t = 0$, the temperature profile of the neighboring solid at the end of each time-step, which is the initial condition for the next time-step, is not uniform anymore, and is given by Eq. (16) for the first time-step. However, using this expression as the initial condition for the next time-step increases the complication of the problem and impedes the analytical solution. To overcome this issue, we represent the temperature profile within the solid boundary at the end of each time-step with an exponential function such that it can be used as an initial condition for the next time-step:

$$T_s(x, 0) = T_\infty + a e^{-bx}, \quad (17)$$

where a and b are coefficients fitted from the computational data. This approach enables us to solve the problem analytically. Since the temperature profile is an error-function type solution, this substitution can satisfy the boundary conditions nicely and

fit the temperature profile accurately. Therefore, the analytical solutions for temperature distribution in both media become:

$$T_f(x, t) = T_H - \frac{T_H - T_\infty}{1 + \sigma} \left\{ \sum_{n=0}^{\infty} \beta^n \left[\operatorname{erfc} \left(\frac{2nl - x}{2\sqrt{\alpha_f t}} \right) - \operatorname{erfc} \left(\frac{2(n+1)l + x}{2\sqrt{\alpha_f t}} \right) \right] \right\} + \frac{a}{1 + \sigma} \left\{ \sum_{n=0}^{\infty} \beta^n e^{h(2nl - x) + h^2 \alpha_f t} \left[\operatorname{erfc} \left(\frac{2nl - x}{2\sqrt{\alpha_f t}} + h\sqrt{\alpha_f t} \right) - e^{2h(n+1)l} \operatorname{erfc} \left(\frac{2(n+1)l + x}{2\sqrt{\alpha_f t}} + h\sqrt{\alpha_f t} \right) \right] \right\}, \quad (18)$$

$$T_s(x, t) = T_\infty + \frac{(T_H - T_\infty)\sigma}{1 + \sigma} \left[\operatorname{erfc} \left(\frac{\gamma x}{2\sqrt{\alpha_f t}} \right) + (\beta + 1) \sum_{n=1}^{\infty} \beta^{n-1} \operatorname{erfc} \left(\frac{2nl + \gamma x}{2\sqrt{\alpha_f t}} \right) \right] - \frac{a\sigma}{1 + \sigma} \left[e^{h\gamma x + h^2 \alpha_f t} \operatorname{erfc} \left(\frac{\gamma x}{2\sqrt{\alpha_f t}} + h\sqrt{\alpha_f t} \right) + (\beta + 1) \sum_{n=1}^{\infty} \beta^{n-1} e^{h(2nl + \gamma x) + h^2 \alpha_f t} \operatorname{erfc} \left(\frac{2nl + \gamma x}{2\sqrt{\alpha_f t}} + h\sqrt{\alpha_f t} \right) \right] + \frac{1}{2} a e^{-bx + \eta t} \left[e^{2bx} \operatorname{erfc} \left(\frac{\gamma x}{2\sqrt{\alpha_f t}} + \sqrt{\eta t} \right) + \operatorname{erfc} \left(\frac{-\gamma x}{2\sqrt{\alpha_f t}} + \sqrt{\eta t} \right) \right], \quad (19)$$

where $\eta = \alpha_s b^2$, and $h = b/\gamma$. These two expressions provide the one-dimensional temperature distribution perpendicular to the wall. If we apply this procedure to all the cells sharing an interface with the wall, we can have an approximation of the temperature distribution all over the solid boundary. This solution can also give an approximation of the thermal boundary layer thickness in both media.

It should be noted that the temperature profiles strongly depend on the thermal properties of the fluid and the neighboring wall, including heat conductivity and diffusivity of the corresponding materials. Since polyurea and steel are of particular interest in naval applications, we applied this analysis to shock-induced collapse of a single bubble near a rigid wall made of these specific materials. Fig. 8 shows the maximum temperature of the wall surface for polyurea as function of initial bubble stand-off and for three different shock strength. It can be seen that the maximum surface temperature is highly dependent on the initial location of the bubble, as well as

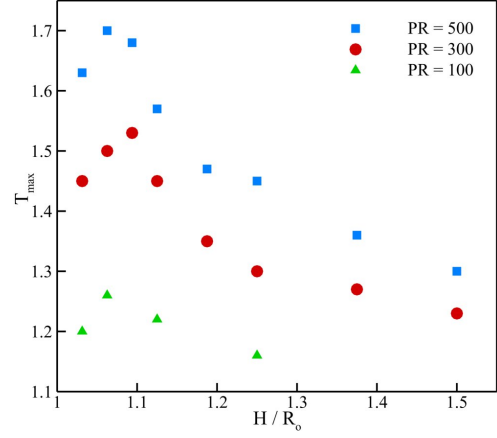


Figure 8: Maximum surface temperature for a polyurea-like material for different shock pressure as a function of H/R_o .

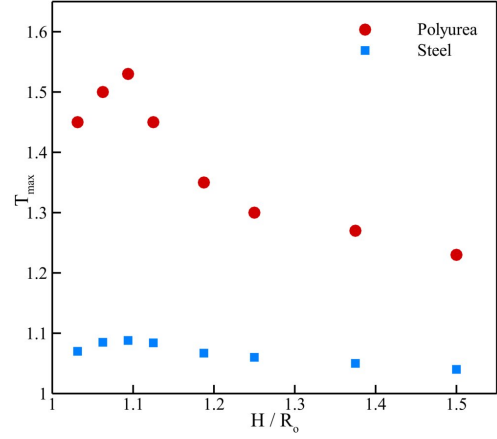


Figure 9: Maximum surface temperature for a polyurea-like material vs. steel as a function of H/R_o with $PR = 300$.

the shock strength. Because of the low heat diffusivity of polyurea, the amount of heat accumulated on the surface of the neighboring wall can be significant which results in an increase in the surface temperature and may eventually melt the polyurea (the melting point for polyurea is in the range of 480 – 620 K based on its molecular structure). This phenomenon may amplify the undesirable effects of cavitation erosion in naval applications.

Fig. 9, which compares the maximum surface temperature for polyurea versus steel, demonstrates that the increase in the surface temperature of steel is not significant, since this material has a relatively large heat diffusivity and would pass the amount of heat transferred from the flow throughout the body of the neighboring wall. Fig. 10 plots the temperature dis-

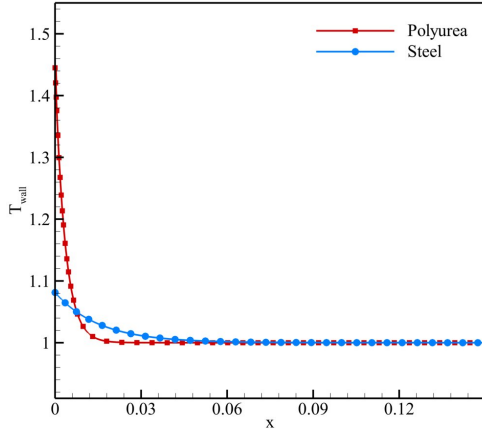


Figure 10: Temperature distribution within the solid boundary for a polyurea-like material vs. steel.

tribution in both polyurea and steel. Following the same argument as above, it can be observed that the thermal boundary layer in polyurea is much thinner than steel. According to these results, surface temperature is not problematic for materials with high heat diffusivity and melting point (e.g., metals), but it will likely be an important factor for softer materials with low heat diffusivity and melting point (e.g., polymers), and may thus be responsible for thermal damage.

3.1.3 2D SIMULATIONS OF SINGLE-BUBBLE COLLAPSE NEAR A COMPLIANT OBJECT

We consider the collapse of an initially cylindrical air bubble in equilibrium with the surrounding medium (i.e., water), located at an initial distance H away from the compliant object. The compliant object has a thickness of T with a wall boundary condition at the end of the layer. The schematic of this two-dimensional problem setup is shown in Fig. 11, and is inspired from the experiments of Swantek & Austin (2010). The shock wave propagates toward the bubble and causes the bubble's collapse. An initial bubble radius of $500 \mu\text{m}$ was used for these simulations. Due to the symmetry, half of the domain is simulated with symmetric boundary condition. Two media are considered for the compliant object: (1) water as a baseline case and (2) polyurea. For the polyurea case, the material is modeled using the following approximated property values: $\rho = 1190 \text{ kg/m}^3$, $\kappa = 0.58 \text{ W/m/K}$, $\mu_B = \mu_s = 0.5 \text{ Pa s}$ and the values in Table 1. We use a uniform Cartesian grid with the resolution of

784×384 corresponding to 128 cells per initial bubble radius.

Fig. 12 shows four different frames of the bubble collapsing and its interaction with the compliant object (polyurea in this instance). Additionally, Figs. 13 and 14 show the bubble jet velocity, bubble centroid x -location, and the water-compliant object x -location along the symmetry line as functions time during the simulation.

In frame 1, the right-moving shock wave has interacted with the bubble and compliant object, and the bubble begins to collapse. Due to the acoustic impedance mismatch between the water and the compliant object, part of the right-moving shock wave is reflected as a shock wave back towards the bubble and part is transmitted into the compliant object. The transmitted shock wave is subsequently reflected by the wall towards the bubble. As the bubble begins to collapse, the transmitted and reflected shock wave interacts with the bubble, and the surrounding material, including the compliant material, are entrained towards the bubble. The deformation of the interface between the water and the compliant object is shown in frame 2 and in Fig. 14 as the bubble centroid and object's x -location approach each other from $t = [0, 3]$. As seen in the three-dimensional case, frame 3 shows the results of the bubble collapsing: a re-entrant jet directed toward the compliant object is produced and an outward propagating shock wave is generated. This strong shock wave then deforms the compliant object's interface away from the bubble. Again, part of the wave is reflected and transmitted into the compliant layer. The transmitted shock wave is then reflected by the wall and its effect is noticeable as a second pressure peak in Fig. 22 after the first peak of the initial collapse. Fig. 14 shows that the case where polyurea is the compliant object produces higher re-entrant jet velocities, and thus

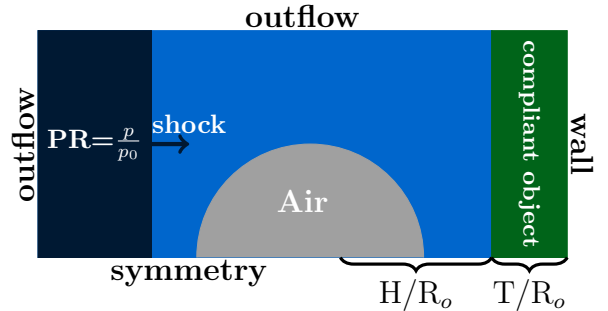


Figure 11: Problem set-up for the shock-induced collapse of an initially cylindrical gas bubble near a compliant object.

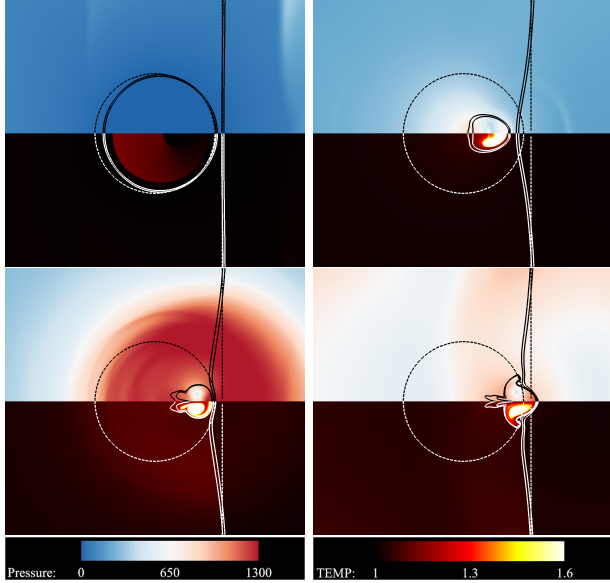


Figure 12: Pressure (top) and temperature (bottom) contours for the 2D shock-induced bubble collapse near a compliant object. Contour lines represent the material interface approximate locations.

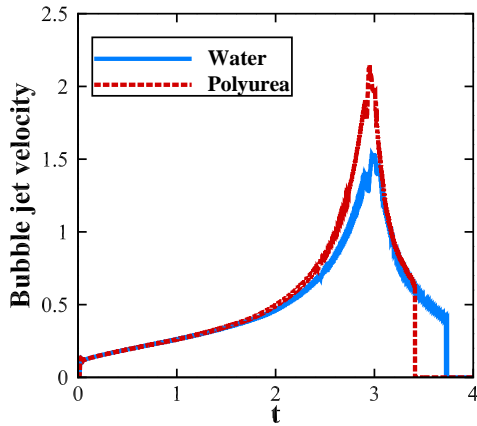


Figure 13: Bubble jet velocities as a function of time for the 2D shock-induced bubble collapse near a compliant object.

a strong bubble collapse, relative to the water case. This results from the acoustic impedance mismatch and the two reflected shock waves interacting with the bubble during its collapse, further increasing the violence of the bubble collapse for the polyurea case. After the bubble's collapse in frame 3, the bubble becomes a hot vortex ring that approaches and further deforms the compliant object in frame 4. From $t = [3, 5]$, Fig. 14 shows that due to the elasticity in the Kelvin-Voigt model, i.e., Eq. (6), the deforma-

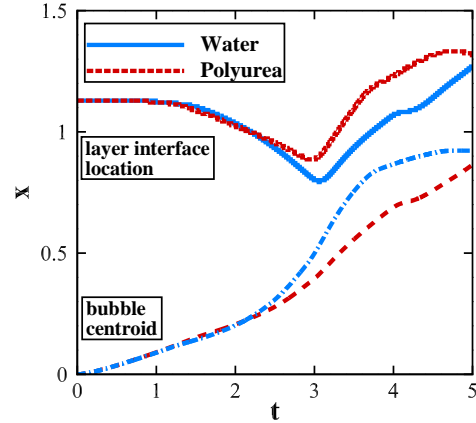


Figure 14: Bubble centroid x -location and water-compliant object interface location as functions of time for the 2D shock-induced bubble collapse near a compliant object.

tion of the polyurea is reduced relative to the water case for the compliant object despite the stronger bubble collapse in the polyurea case. Moreover, the curvature in the object interface x -location in the polyurea case from $t = [3, 5]$ demonstrates the compliant object's return towards the initial location representative of the elastic behavior in the Kelvin-Voigt model used for the polyurea. These results demonstrate the significant and active role that a compliant object's acoustic impedance and elasticity play in the deformations experienced by the neighboring surface. The pressure and temperature response in the compliant object as a function of time for this single bubble case are presented in section 3.2.2. Comparable results of the thermal response in the compliant layer with the three-dimensional single bubble collapse near a rigid wall in section 3.1.1 are not expected. This was due to the compliant object being able to deform and thus not having infinite acoustic impedance as was the case with the rigid wall, thus resulting in different bubble dynamics between the two problems.

3.2 MULTIPLE-BUBBLE COLLAPSE

Although studying single bubble collapse is valuable to explore the physics of the collapse, the bubble-bubble interactions, occurring for instance during the collapse of bubble clouds, are important factors in cavitation erosion. At the present time, capturing such bubble-bubble interactions is beyond the reach of even the most sophisticated cloud models (Fuster & Colonius, 2011). For this reason, we perform three-

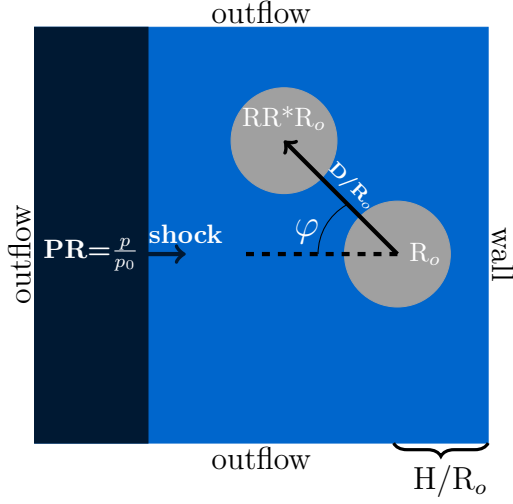


Figure 15: Problem set-up for the shock-induced collapse of two initially spherical gas bubbles near a rigid surface.

and two-dimensional simulations of multiple-bubbles collapsing near rigid/compliant surface in order to study the effects of bubble-bubble interactions on the collapse dynamics.

3.2.1 3D SIMULATIONS OF MULTIPLE-BUBBLE COLLAPSE NEAR A RIGID WALL

We study the collapse of two initially spherical bubbles located near a rigid wall. Fig. 15 shows a 2D schematic of the 3D problem setup. We have a uniform Cartesian grid with the resolution of $1200 \times 480 \times 880$ (160 cells per bubble radius at $t = 0$).

Here, we only simulate half of the domain due to the axisymmetry of the problem with respect to the xz -plane. The right-most (primary) bubble is located at an initial distance H away from the wall. The initial distance between the two bubbles is denoted by D and ϕ defines the angle between the line that connects the bubbles' initial centroids and the horizontal. For this problem, $D = 2.5$. RR indicates the radius ratio of the secondary bubble with reference to the radius of the front bubble. Unless mentioned otherwise, $RR = 1$ will be the radius ratio for all multiple-bubble collapse problems in this work.

Fig. 16 shows three different 2D contours (middle plane) of the collapse process of the base problem for $\phi = 45^\circ$. Similar to the single-bubble case, the right-moving shock interacts with the bubbles and creates strong rarefaction waves (frame 1). Due to the interactions between the bubbles and the waves,

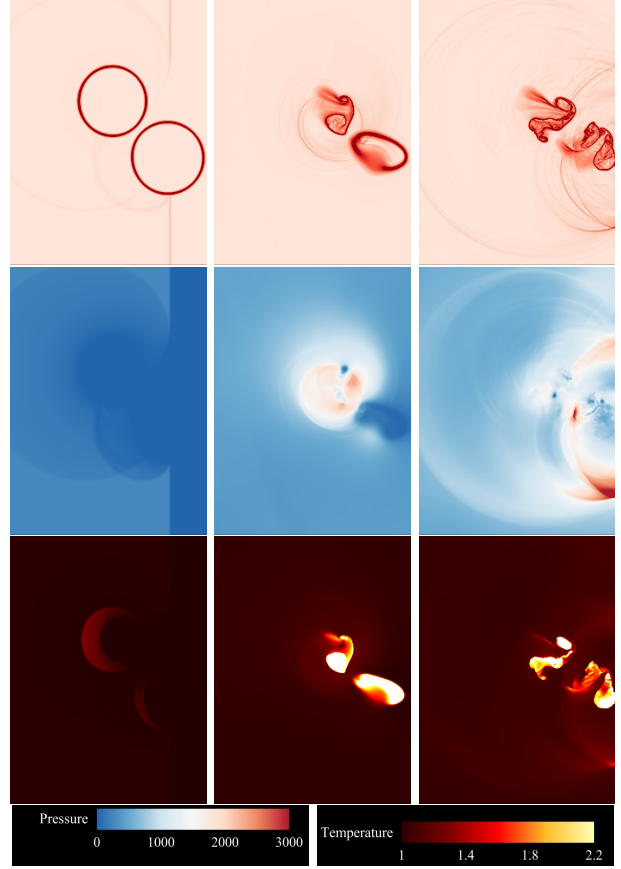


Figure 16: Density gradient magnitude (top), pressure (middle) and temperature (bottom) contours for the base 3D shock-induced bubble collapse problem near a rigid surface.

the secondary bubble (the one initially farther away from the wall) collapses, while the front bubble is deforming and creating the re-entrant jet. The shock wave from the collapse of the secondary bubble interacts with the other bubble, and boosts its collapse (frame 2). The primary bubble collapses and generates a strong shock wave. The collapsed bubbles take the form of hot vortex rings and convect toward the wall (frame 3). The bubble-bubble interactions increase the non-sphericity of the collapse and lead to a very more complicated process than the collapse of a single bubble. These interactions may increase or decrease the collapse intensity depending on the flow configuration.

Fig. 17 shows the maximum wall pressure and temperature as a function of the angle, with a comparison to single-bubble collapse. It should be first noted that the configuration can amplify or reduce the wall pressure. The underlying reason is that the wave dy-

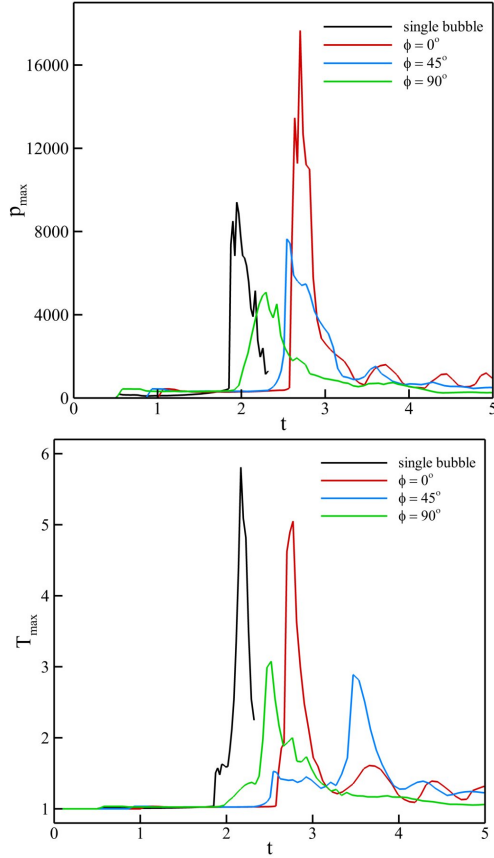


Figure 17: Maximum wall pressure (top) and temperature (bottom) plots on the wall as a function of time for different ϕ .

namics (shock interaction with the secondary bubble, reflected rarefaction) give rise to a higher or lower collapse pressure for the primary bubble. The configuration that produces the highest pressure is the case where the bubbles are lined up, in which case the collapse of the primary bubble is driven by both the incoming shock and the shock produced by the secondary bubble. On the other hand, the maximum wall temperature strongly depends on the configuration, specifically the proximity of the primary bubble at collapse from the wall.

According to Fig. 17, it can be concluded that bubble-bubble interactions have significant effects on the maximum pressure and temperature along the wall. Depending on the angle ϕ , the maximum pressure may be amplified or decreased. Temperature seems to behave in the same fashion, but with a more complicated behavior since the interactions between the bubbles affect the vortex ring migration toward the wall and subsequently the temperature behavior. This can be seen better in Fig. 18 where maximum

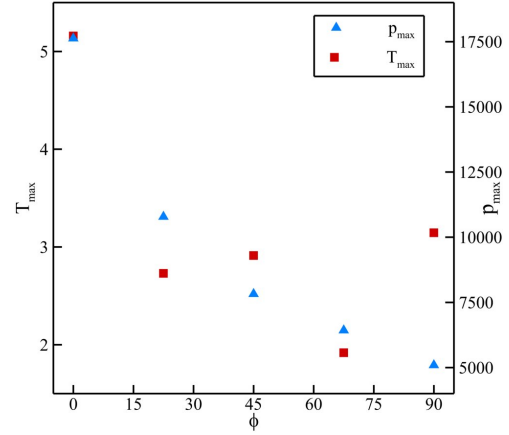


Figure 18: Maximum pressure and temperature on the wall as a function ϕ .

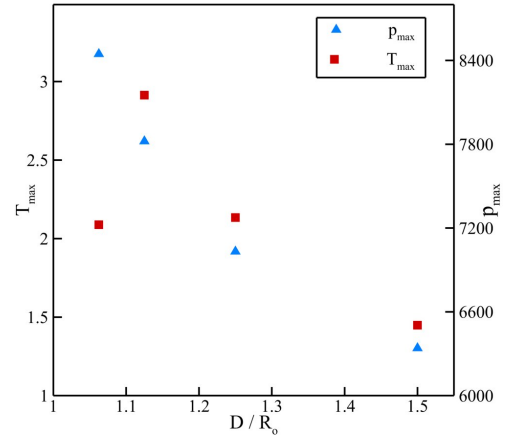


Figure 19: Maximum pressure and temperature on the wall as a function D/R_o , where $H/R_o = 1.125$ and $\phi = 45^\circ$.

pressure and temperature are plotted as a function of ϕ . The maximum pressure decreases as the bubbles go from “one behind the other” ($\phi = 0^\circ$) to “side-by-side” ($\phi = 90^\circ$), while the maximum temperature does not obey the same behavior.

Fig. 19 compares maximum pressure and temperature on the wall for different distances between the two bubbles. Overall, maximum wall pressure and temperature decrease as the bubbles get farther apart. This is expected since the amplitude of the shock produced by the secondary bubble collapse decreases with distance from the primary bubble (Johnsen & Colonius, 2009).

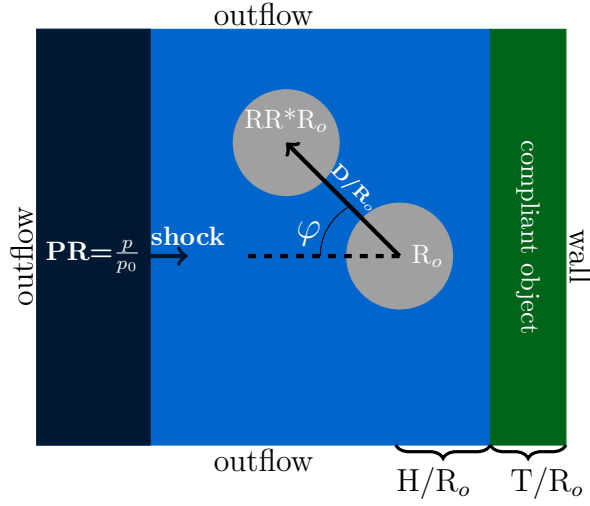


Figure 20: Problem set-up for the shock-induced collapse of two initially cylindrical gas bubbles near a compliant object.

3.2.2 2D SIMULATIONS OF MULTIPLE-BUBBLE COLLAPSE NEAR A COMPLIANT OBJECT

Similar to the previous problem with two bubbles near a rigid wall, we conduct a 2D study of two gas bubbles collapsing near a compliant object. Fig. 20 shows the problem setup. The two bubbles are initially cylindrical and in equilibrium with the surrounding water with the front (primary) bubble located a distance H away from the compliant object of thickness T . Only polyurea is considered as the compliant object in this study with the same material properties as mentioned in section 3.1.3.

As before, RR indicates the radius ratio of the secondary bubble with reference to the radius of the front bubble, D the initial distance from the center of the front bubble to the back bubble, and ϕ the angle between the line that connects the bubbles' initial centroids and the horizon. $D = 2.5$ for this problem. We have a uniform Cartesian grid with a resolution that varies with ϕ such that there was 128 cells per initial bubble radius, for example, for $\phi = 45^\circ$ has a resolution of 1010×994 .

Fig. 21 shows three different contours of the two bubbles collapsing for the case with $\phi = 45^\circ$ near the compliant object. The maximum pressures and temperatures as a function of time for three values of ϕ are presented in Fig. 22. The single bubble results are also presented for comparison with the two bubble configuration.

Similar to the single bubble problem in section 3.1.3, the right-moving shock wave interacts with

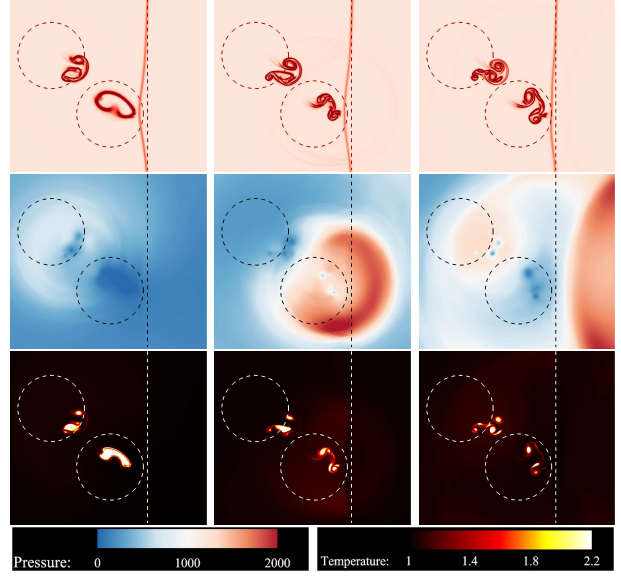


Figure 21: Density gradient magnitude (top), pressure (middle) and temperature (bottom) contours for the 2D shock-induced bubble collapse base problem near a compliant object.

the two bubbles and advects towards the compliant object. Part of the shock wave is reflected back towards the two bubbles and the rest is transmitted into the polyurea due to the acoustic impedance mismatch between the water and polyurea. Due to the proximity of the shock wave with the secondary bubble (the one initially farther away from the wall) at the start of the simulation, the secondary bubble collapses first while the primary bubble is deforming and creating the re-entrant jet. The shock wave timing delay due to the secondary bubble location is also noticeable in the polyurea's pressure and temperature responses in Fig. 22 for $t = [0, 2]$ between ϕ angles. Thereafter, frame 1 shows how the secondary bubble collapses and emits a shock wave that interacts with the primary bubble. The interaction takes place during the primary bubble's collapse and, as a result, strengthens the primary bubble's collapse and emitted shock wave seen in frames 2 and 3. It is noted that, as the primary bubble collapses, the deformation of the water-polyurea interface is most noticeable due to entrainment of material as the bubble decreases in volume.

As the shock wave is partially reflected and transmitted into the polyurea, it produces a second maximum pressure and temperature peak. As seen in the previous problems, frame 3 shows the bubbles forming into hot convecting vortex rings that approach and deform the compliant layer. Similar bubble-bubble interactions that further the asymmetry of

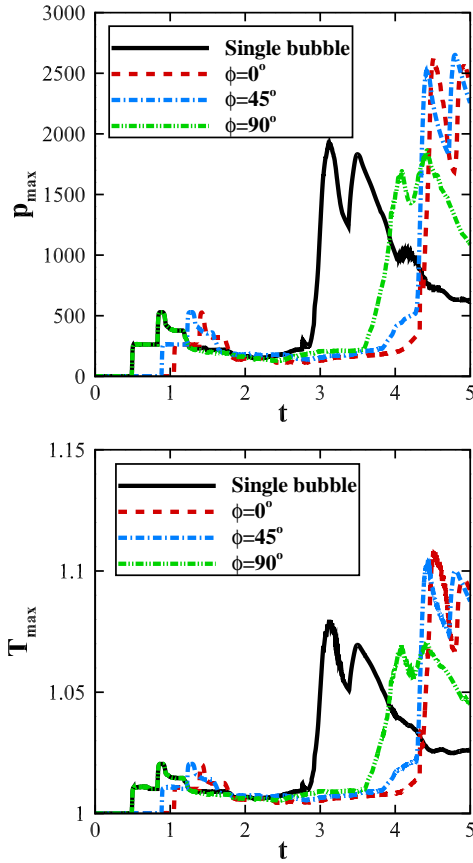


Figure 22: Maximum pressure (top) and temperature (bottom) in the compliant object as a function time for various cases of ϕ .

the bubbles' shape, relative the single bubble, as they collapse, are noticed. This can be seen in the three-dimensional results in section 3.2.1. This interaction is most noticeable in the delayed and slightly reduced pressure and temperature response for the case where $\phi = 90^\circ$ which is the most comparable to the single bubble case. Also, for the $\phi < 90^\circ$ cases, the maximum pressures and temperatures experienced in the polyurea are similarly increased relative to the $\phi = 90^\circ$ and single bubble configurations.

4 CONCLUSIONS

To provide a better understanding of cavitation erosion, we carried out high-fidelity numerical simulations of two- and three-dimensional shock-induced collapse of a gas bubble in the vicinity of a rigid/compliant wall for different geometrical configurations. We investigated the detailed flow physics of the problem with an emphasis on temperature effects for bubble collapse near a rigid surface, as well

as wave propagation and viscoelastic effects for bubble collapse near a compliant surface. We showed that the initial location of the bubble plays a critical role in the collapse dynamics that as the bubble gets closer to the wall. We also illustrated that if the bubble is close enough to the wall the maximum temperature measured on the neighboring surface is caused by the hot vortex ring convecting toward that surface, which is significantly higher than the maximum wall temperature caused by the shock wave from the collapse. In addition, we introduced an analytical heat transfer model to estimate the actual temperature of the wall using our three-dimensional flow simulations. The acoustic impedance mismatch between the surrounding fluid and the compliant object and the viscoelasticity of the material were shown to play a key role in the bubble collapse strength and deformation of the compliant object's interface. In particular, the acoustic impedance mismatch between the surround fluid and compliant object led to a higher re-entrant jet velocity relative to the water case surrounding the bubble. Additionally, we simulated the shock-induced collapse of multiple bubbles near a rigid/compliant surface. We demonstrated that strong bubble-bubble interactions may significantly affect the dynamics of the flow: amplify/reduce pressures and temperatures produced at the collapse, and increase the non-sphericity of the bubbles as they collapse and the collapse time. This work will be continued to explore and analyze more detailed physics of cavitation bubble collapse.

ACKNOWLEDGEMENTS

This work was supported in part by ONR grant N00014-12-1-0751 under Dr. Ki-Han Kim. We also used the Extreme Science and Engineering Discovery Environment (XSEDE), which is supported by National Science Foundation grant number ACI-1053575.

REFERENCES

- R. Abgrall, How to prevent pressure oscillations in multicomponent flow calculations: a quasi conservative approach, *J. Comput. Phys.* 125 (1996) 150–160.
- M.R. Amini, J. Simon and S. Nemat-Nasser, Numerical modeling of effect of polyurea on response of steel plates to impulsive loads in direct pressure-pulse experiments, *Mech. Mater.* 42 (2010) 615–627.
- G. J. Ball, B. P. Howell, T. G. Leighton and M. J. Schofield, Shock-induced collapse of a cylindrical air

- cavity in water: a Free-Lagrange simulation, *Shock Waves* 10 (2000) 265–276.
- S. Alahyari Beig and E. Johnsen, Maintaining interface equilibrium conditions in compressible multiphase flows using interface capturing, *J. Comput. Phys.* 302 (2015) 548–566.
- S. Alahyari Beig and E. Johnsen, Temperature considerations in non-spherical bubble collapse near a rigid wall, *J. Phys.: Conf. Ser.* 656 (2015) 012044.
- T. B. Benjamin and A. T. Ellis, The collapse of cavitation bubbles and the pressures thereby produced against solid boundaries, *Phil. Trans. Roy Soc. London A* 260 (1966) 221–240.
- J. R. Blake and D. C. Gibson, Cavitation Bubbles Near Boundaries, *Annu. Rev. Fluid Mech.* 19 (1987) 99–123.
- N. K. Bourne and J. E. Field, Shock-induced collapse of single cavities in liquids, *J. Fluid Mech.* 244 (1992) 225–240.
- M. Brenner, S. Hilgenfeldt and D. Lohse, Single-bubble sonoluminescence, *Rev. Mod. Phys.* 74 (2002) 425 – 484.
- V. Coralic and T. Colonius, Finite-volume WENO scheme for viscous compressible multicomponent flows, *J. Comput. Phys.* 274 (2014) 95–121.
- J. M. Carcione, *Wave Fields in Real Media, Third Edition: Wave Propagation in Anisotropic, Anelastic, 353 Porous and Electromagnetic Media*, 3rd ed., Elsevier Science, 2014.
- H.S. Fogler and J.D. Goddard, Collapse of spherical cavities in viscoelastic fluids, *Phys. Fluids.* 13 (1970) 1135–1141.
- J. P. Franc, M. Riondet, A. Karimi and G. L. Chahine, Material and velocity effects on cavitation erosion pitting, *Wear* 274–275 (2012) 248–259.
- Y.-C. Fung, *Biomechanics*, 1993.
- D. Fuster and T. Colonius, Modelling bubble clusters in compressible liquids, *J. Fluid Mech.* 688 (2011) 352–389.
- R. Gaudron, M.T. Warnez and E. Johnsen, Bubble dynamics in a viscoelastic medium with nonlinear elasticity, *J. Fluid Mech.* 766 (2015) 54–75.
- S. L. Gavriluk, N. Favrie and R. Saurel, Modelling wave dynamics of compressible elastic materials, *Journal 370 of Computational Physics* 227 (2008) 2941–2969.
- S. Gottlieb and C. W. Shu, Total variation diminishing Runge-Kutta schemes, *Math. Comput.* 67 (1996) 73–85.
- S. Hattori, E. Benitani, W. Ruan, Y. Suda, R. Takeuchi and T. Iwata, Cavitation erosion of low-density polyethylene coatings for pipe liners, *J. Phys.: Conf. Ser.* 656 (2015) 012048.
- N A. Hawker and Y. Ventikos, Interaction of a strong shockwave with a gas bubble in a liquid medium: a numerical study, *J. Fluid Mech.* 701 (2012) 59–97.
- M. T. Henry de Frahan, V. Varadan and E. Johnsen, A new limiting procedure for discontinuous Galerkin methods applied to compressible multiphase flows with shocks and interfaces, *J. Comput. Phys.* 280 (2015) 489–509.
- C. Hua and E. Johnsen, Nonlinear oscillations following the Rayleigh collapse of a gas bubble in a linear viscoelastic (tissue-like) medium, *Phys. Fluids.* 25 (2013).
- G. S. Jiang and C. W. Shu, Efficient implementation of weighted ENO schemes, *J. Comput. Phys.* 228 (1996) 202–228.
- E. Johnsen and T. Colonius, Implementation of WENO schemes in compressible multicomponent flow problems, *J. Comput. Phys.* 219 (2006) 715–732.
- E. Johnsen and T. Colonius, Numerical simulations of non-spherical bubble collapse, *J. Fluid Mech.* 629 (2009) 231–262.
- E. Johnsen and F. Ham, Preventing numerical errors generated by interface-capturing schemes in compressible multi-material flows, *J. Comput. Phys.* 231 (2012) 5705–5717.
- J. B. Keller and M. Miksis, Bubble oscillations of large-amplitude, *J. Acoust. Soc. Am.* 68 (2) (1980) 628–633.
- K. H. Kim, G. Chahine, J. P. Franc and A. Karimi, *Advanced experimental and numerical techniques for cavitation erosion Prediction*, Vol. 106, Springer, Netherlands, 2014.
- R. T. Knapp, Recent investigations of the mechanics of cavitation and cavitation damage, *Trans. Am. Soc. Mech. Engrs* 77 (1955) 1045–1054.
- M. Kornfeld and L. Suvorov, On the destructive action of cavitation, *J. Appl. Phys.* 15 (1944) 495–506.

- A. Kulikovskii, N. Pogorelov, A. Semenov and K. Piechor, Mathematical Aspects of Numerical Solution 408 of Hyperbolic Systems. Monographs and Surveys in Pure and Applied Mathematics, Vol. 118, Applied 409 Mechanics Reviews 55 (3) (2002) B46.
- W. Lauterborn and H. Bolle, Experimental investigations of cavitation bubble collapse in the neighborhood of a solid boundary, J. Fluid Mech. 72 (1975) 391–399.
- W. Lauterborn and T. Kurz, Physics of bubble oscillations, Rep. Prog. Phys. 73 (2010) 106501.
- O. Le Metayer, J. Massoni and R. Saurel, Modelling evaporation fronts with reactive Riemann solvers, J. Comput. Phys., 205 (2005) 567–610.
- O. Lindau and W. Lauterborn, Cinematographic observation of the collapse and rebound of a laser-produced cavitation bubble near a wall, J. Fluid Mech. 479 (2003) 327–348.
- P. Movahed and E. Johnsen, A solution-adaptive method for efficient compressible multifluid simulations, with application to the Richtmyer-Meshkov instability, J. Comput. Phys. 239 (2013) 166–186.
- R. R. Nourgaliev, T. N. Dinh and T. G. Theofanous, Adaptive characteristics-based matching for compressible multifluid dynamics, J. Comput. Phys. 213 (2006) 500–529.
- A. Philip and W. Lauterborn, Cavitation erosion by single laser-produced bubbles, J. Fluid Mech. 361 (1998) 75–116.
- J. Qiao, A. V. Amirkhizi, K. Schaaf, S. Nemat-Nasser and G. Wu, Dynamic mechanical and ultrasonic properties of polyurea, Mech. Mater. 43 (2011) 598–607.
- M. Rodriguez and E. Johnsen, A high-order finite-difference method for numerical simulations of shock waves in heterogeneous, linear viscoelastic media. Submitted (2016).
- A. Samiee, A. V. Amirkhizi and S. Nemat-Nasser, Numerical study of the effect of polyurea on the performance of steel plates under blast loads, Mech. Mater. 64 (2013) 1 – 10.
- K. M. Shyue, An efficient shock-capturing algorithm for compressible multicomponent problems. J. Comput. Phys. 142 (1998) 208–242.
- A. B. Swantek and J. M. Austin, Collapse of void arrays under stress wave loading, J. Fluid. Mech. 649 (2010) 399–427.
- I. Tanasawa and W.J. Yang, Dynamic behavior of a gas bubble in viscoelastic liquids, J. Appl. Phys. 41 (1970) 4526–4531.
- Y. Tomita and A. Shima, Mechanisms of impulsive pressure generation and damage pit formation by bubble collapse, J. Fluid Mech. 169 (1986) 535–564.
- X. Yang and C.C. Church, A model for the dynamics of gas bubbles in soft tissue., J. Acoust. Soc. Am. 118 (2005) 3595–3606.

DISCUSSIONS

Jean-Pierre Franc

Laboratory of Industrial and Geophysical Flows,
 Grenoble University, LEGI, BP 53, 38041 Grenoble
 Cedex 9, France.

This work is a very valuable contribution to the understanding of the mechanisms of cavitation erosion. One of the original features of this work is that it includes not only the mechanical loading of the wall due to bubble collapse, but also the thermal loading, which is rarely the case. This issue is particularly relevant for compliant walls made e.g. of polymers that have usually a low heat diffusivity and a relatively low melting point and that, as a result, may behave quite differently from metallic materials.

The paper investigates numerically a large number of cases including single and multiple bubble collapse, near a rigid and compliant wall and several key results are given. The authors show that the liquid temperature on the wall may raise either because of the shock wave produced at bubble collapse or because of the high temperature reached within the remaining part of the compressed bubble and that the latter mechanism becomes predominant at low standoff distances. An analytical thermal model that accounts for the thermal boundary layer at the liquid/solid interface was developed, that makes it possible to estimate the wall temperature of the solid. The authors show that the maximum surface temperature is significantly higher in the case of polyurea compared to steel and that it depends notably upon the standoff distance. Moreover, the analysis of the collapse of two bubbles near a rigid and a compliant wall provides an essential insight into bubble-bubble Interactions.

1. The model developed by the authors assumes no mass transfer through the bubble wall. The bubble is supposed to contain air that is non condensable unlike water vapor. Does this assumption introduce a bias when modeling an actual cavitation bubble that is expected to contain water vapor together with a variable quantity of non-condensable gas depending upon the air content in water?
2. In order to model the compliant wall, the Kelvin-Voigt viscoelastic model is used. When the bubble has collapsed and the stress is released, the material progressively relaxes to its original undeformed state. Would it be possible to introduce other types of models for the solid that

would account for a permanent residual deformation after bubble collapse?

3. The viscoelastic material is expected to dissipate energy. How does the loss of energy in the compliant material compare to the potential energy of the collapsing cavitation bubble? What is the impact of energy dissipation on the material local temperature? Since the viscoelastic properties may depend upon temperature, can this be included in the model and can we expect a significant influence of temperature via material properties on flow dynamics and material behavior?
4. In the case of 2D simulations of single-bubble collapse near a compliant wall, the authors show that the collapse of the bubble produces a higher re-entrant jet and thus a stronger collapse in comparison to water (see Fig.13). Could the authors explain what the baseline case of water is exactly and if it actually corresponds to the case of a rigid wall or not? What is the physical mechanism that makes the collapse near a polyurea wall more violent?
5. When the distance to the wall decreases, the maximum wall temperature first increases as a result of the heating by the closer and closer hot vortex ring and then decreases as shown in Fig. 8. Can the authors explain why the maximum temperature decreases at small standoff distances and why a maximum is predicted at a given standoff distance?
6. In the case of the collapse of a two-bubble system, the authors show that the maximum wall pressure and temperature may be increased or decreased in comparison to single bubble collapse depending upon the relative position between the two bubbles and their position relatively to the wall. Is there a key parameter that governs the aggressiveness of the configuration and that would help deciding a priori whether a given configuration is more or less aggressive than the single bubble case?

Congratulations for this excellent piece of numerical work that includes several original results and conclusions and is very instructive on the mechanisms involved in cavitation erosion.

AUTHOR'S REPLY

The authors appreciate the thoughtful and insightful questions. Detailed answers are included below.

Question 1: For the problems under consideration, we expect that mass transfer may affect the heat transfer (phase change) or temperature fields. However, since the bubble collapse is non-spherical and does not achieve exceedingly small sizes and is inertia-dominated, we do not expect mass transfer to significantly influence the dynamics or pressures. We are currently working toward incorporating mass transfer to our computational framework.

Question 2: Other models can and have been introduced into the present computational framework. The (linear) Kelvin-Voigt model used in the present work is applicable to small strains. Stress relaxation has also been included but is not investigated here. We expect that plasticity (permanent deformation mechanisms) can also readily be incorporated. The main difficulty lies in the implementation of additional physics/models, because evolution equations are required for the different components of the stress tensor. We are currently implementing additional models, including nonlinear elasticity.

Question 3: The present linear Kelvin-Voigt model includes viscoelastic dissipation, which is solely viscous in this case. The focus of the present work was to understand the role of specific viscoelastic effects by isolating them in a generic framework, rather than seek to represent a given material as accurately as possible (in terms of constitutive relation and equation of state). We believe this approach to be better suited to producing fundamental knowledge applicable to a wide range of problems/materials. As noted in point 2, more sophisticated constitutive models could be included to account for coupling between the thermodynamics and the deformations. We are in fact working toward including such effects into our computational framework.

Question 4: The baseline case of water for the 2D simulations of a single-bubble collapse near a compliant wall is the same geometry as that for the compliant object with the exception that the region with the compliant object is water. Thus, there is no wave reflection (due to the acoustic impedance mismatch) back onto the bubble, which in the case of a shock (i.e., if the material is “hard”) would increase the effective pressure driving the bubble collapse. Furthermore, the initial distance of the bubble from the wall H is greater in the 2D simulations than in 3D; additionally, 3D geometries give rise to more focusing and more violent collapse.

Question 5: It should be noted that in Fig. 8 the maximum temperature measured on the wall locally increases by increasing the initial bubble stand-off, not the maximum temperature of the bubble. In fact, the maximum temperature measured on the wall

highly depends on the dynamics of the vortex ring. The temperature of the vortex ring is high but non-uniform within the bubble. It convects toward the wall while rotating. Therefore, it is important that when the vortex ring reaches the wall and what part of it is in contact with the wall surface. For those H/R_o cases closest to the wall, the hottest part of the vortex ring does not come in as close contact to the wall due to the evolving bubble/vortex ring dynamics during collapse.

Question 6: We are indeed investigating this problem in greater detail. Given an initial stand-off distance of the proximal bubble from the wall and shock strength, we determined that the angle and the distance between the two bubbles are the two key parameters on which the dynamics and wall pressures/temperatures depend. Additionally, the relative size of the bubbles is another important parameter. At the present time, we are still investigating the basic bubble dynamics, before trying to relate them to experimentally observable flow quantities (e.g., void fractions and pressure driving the collapse).